



Faint and Fading Tails: The Fate of Stripped HI Gas in Virgo Cluster Galaxies

Rhys Taylor¹, Joachim Köppen^{1,2}, Pavel Jáchym¹ , Robert Minchin³ , Jan Palouš¹ , and Richard Wünsch¹ 

¹Astronomical Institute of the Czech Academy of Sciences, Boční II 1401/1a, 141 00 Praha 4, Czech Republic; rhysyt@gmail.com

²Institut für Theoretische Physik und Astrophysik der Universität zu Kiel, D-24098, Kiel, Germany

³Stratospheric Observatory for Infrared Astronomy/USRA, NASA Ames Research Center, MS 232-12, Moffett Field, CA 94035, USA

Received 2019 October 16; revised 2019 December 22; accepted 2019 December 23; published 2020 April 21

Abstract

Although many galaxies in the Virgo cluster are known to have lost significant amounts of HI gas, only about a dozen features are known where the HI extends significantly outside its parent galaxy. Previous numerical simulations have predicted that HI removed by ram pressure stripping should have column densities far in excess of the sensitivity limits of observational surveys. We construct a simple model to try and quantify how many streams we might expect to detect. This accounts for the expected random orientation of the streams in position and velocity space as well as the expected stream length and mass of stripped HI. Using archival data from the Arecibo Galaxy Environment Survey, we search for any streams that might previously have been missed in earlier analyses. We report the confident detection of 10 streams as well as 16 other less-certain detections. We show that these well match our analytic predictions for which galaxies should be actively losing gas; however, the mass of the streams is typically far below the amount of missing HI in their parent galaxies, implying that a phase change and/or dispersal renders the gas undetectable. By estimating the orbital timescales, we estimate that dissolution rates of $1\text{--}10 M_{\odot} \text{ yr}^{-1}$ are able to explain both the presence of a few long, massive streams and the greater number of shorter, less-massive features.

Unified Astronomy Thesaurus concepts: [Galaxy evolution \(594\)](#); [Galaxy dynamics \(591\)](#); [Galaxy clusters \(584\)](#); [Virgo Cluster \(1772\)](#); [Intracluster medium \(858\)](#)

Supporting material: figure set

1. Introduction

It is well-established that many late-type galaxies in Virgo are strongly deficient in HI; that is, they possess less HI gas than similar field galaxies (e.g., Haynes & Giovanelli 1986; Solanes et al. 2001; Gavazzi et al. 2008). In some cases, this is equivalent to a loss of $>6 \times 10^9 M_{\odot}$ (Taylor et al. 2012). It is also well known that a few galaxies in the cluster are associated with spectacular HI streams up to 500 kpc in extent (Koopmann et al. 2008), while others appear to have much shorter features (Chung et al. 2007). There appears to be little or no correlation between which galaxies are deficient and which possess streams. Some of the longest streams are associated with galaxies that are even gas rich, whereas many strongly deficient galaxies apparently lack streams entirely.

The dominant mechanism for gas loss in clusters is thought to be ram pressure stripping (e.g., Gunn & Gott 1972; Vollmer et al. 2001; Jáchym et al. 2007, 2009; Roediger & Brüggén 2008; Köppen et al. 2018, for a detailed review see Boselli & Gavazzi 2006). This can explain the complete removal of the gas content of a massive galaxy in a few orbits, while leaving the stellar component largely unaffected. In contrast, tidal encounters (e.g., Toomre & Toomre 1972; Bekki et al. 2005; Duc & Bournaud 2008) have been shown to more likely result in only small amounts of gas being removed (e.g., Taylor et al. 2017).

Deficiency alone does not necessarily mean that a galaxy is currently losing gas—it may have been stripped in the distant past, and even if close to the cluster center (where ram pressure is expected to be strongest) in projection, its true 3D distance may be significantly greater. Detecting short streams is hampered by the low resolution of single-dish observations, with limited data available from interferometers with the

necessary sensitivity. Physically, once gas is removed from its parent galaxy, it may disperse into a larger volume, and/or it might experience a phase change (either by heating or cooling) and so is rendered undetectable.

Yet collectively, the discrepancy between the numbers of deficient galaxies and those with streams seems too strong to ignore. The Arecibo-based Arecibo Legacy Fast ALFA survey (ALFALFA; Giovanelli et al. 2005) and Arecibo Galaxy Environment Survey (AGES; Auld et al. 2006) projects have both covered parts of the cluster to high sensitivity at 17 kpc resolution. Galaxies of low and high deficiency are found in close proximity to one another, strongly suggesting that at least some galaxies in the surveyed regions should be in the process of actively losing gas (Taylor et al. 2012, see also phase-space investigations, e.g., Jaffé et al. 2015; Rhee et al. 2017). While the earlier Very Large Array (VLA) Imaging of Virgo in Atomic gas survey (VIVA; Chung et al. 2009) discovered several short streams, both Arecibo surveys have reported few new HI streams in Virgo—none at all in the case of AGES.

In principle, a sufficiently rapid phase change could explain the dearth of streams (e.g., Boselli et al. 2019). Yet the existence of a few extremely long streams at least shows that this cannot be the complete explanation. If evaporation does account for the lack of most of the expected streams, why are there any long streams at all—especially near the center of the cluster? Why is there no correlation between the deficiency of a galaxy and the presence of a stream?

This problem has been remarked upon in Oosterloo & van Gorkom (2005), Vollmer & Hutchmeier (2007), and ourselves in Taylor et al. (2016). Oosterloo & van Gorkom (2005) describe a particularly interesting stream—it is approximately 100 kpc long, located near the center of the Virgo cluster, and its length suggests a survival time ~ 100 Myr. Its parent galaxy

Table 1
Properties of Known Optically Dark H I Features in the Virgo Cluster

Name	R.A.	Decl.	Velocity (km s ⁻¹)	Distance (Mpc)	M_{HI} (M_{\odot})	Projected size (kpc)	W50 (km s ⁻¹)	W20 (km s ⁻¹)	Reference
AGESVC1 231	12:18:17.9	07:21:40	191	32	4.2E7	<32	36	152	T12
AGESVC1 247	12:24:59.2	08:22:38	1087	23	2.3E7	<23	22	33	T12
AGESVC1 257	12:36:55.1	07:25:48	1580	17	1.4E7	<17	131	157	T12
AGESVC1 258	12:38:07.2	07:30:45	1786	17	1.4E7	<17	32	120	T12
AGESVC1 262	12:32:27.2	07:51:52	1322	23	2.0E7	<23	104	146	T12
AGESVC1 266	12:36:06.5	08:00:07	1691	17	3.2E7	<17	77	173	T12
AGESVC1 274	12:30:25.6	08:38:05	1297	17	7.3E6	<17	22	35	T12
AGESVC1 282	12:25:24.1	08:16:54	943	23	4.4E7	<23	69	164	T12
AAK2 C1N	12:08:47.6	11:55:57	1234	17	2.0E7	5	22	...	K10
AAK2 C1S	12:08:47.4	11:54:48	1225	17	2.7E7	7	20	...	K10
AAK2 C2N	12:13:42.5	12:54:50	2237	32	3.4E7	23	13	...	K10
AAK2 C2W	12:13:33.1	12:52:44	2205	32	6.0E7	22	41	...	K10
AAK2 C2S	12:13:41.9	12:51:16	2234	32	1.2E7	8	6	...	K10
VCC 1249	12:29:54.4	07:58:05	475	17	5.1E7	<17	29	63	T12
KW cloud	12:28:34.4	09:18:33	1270	17	7.0E7	37	73	...	S17
VCC 865	12:25:58.8	15:40:17	-128	17	7.0E7	13	110	...	C07
VCC 497	12:21:42.5	14:35:54	1149	17	9.0E7	16	50	...	C07
VCC 465	12:21:17.8	11:30:38	355	17	2.0E8	27	110	...	C07
VCC 1516	12:21:40.5	11:30:00	237	17	2.6E8	14	90	...	C07
VCC 630	12:23:17.2	11:22:05	1563	17	4.0E7	13	50	...	C07
VCC 2066	12:47:59.9	10:58:15	1141	17	9.0E8	50	78	...	D07
VCC 979	12:27:11.6	09:25:14	437	23	4.3E7	60	50	...	S17
VCC 1987	12:43:56.6	13:07:36	1046	17	4.1E8	32	90	...	C07
AA Virgo 7	12:30:25.8	09:28:01	488	17	5.3E8	173	127	...	K09
VIRGOHI21	12:17:52.9	14:47:19	2005	17	1.8E8	250	463	...	M07
HI1225 + 01	12:27:46.3	01:36:01	1292	17	2.9E9	182	60	...	G89
VCC 836 plume	12:25:46.7	12:39:44	2524	17	3.8E8	124	550	...	O05
Koopmann	12:34:19.3	06:28:04	2012	17	4.0E8	500	290	...	K08

Note. The “name” column gives the parent galaxy (where available). Spatial coordinates are in J2000. All parameters, except coordinates, refer to the optically dark gas and not the parent galaxy (if one is present). We divide the table into three categories, separated by horizontal lines: the upper section contains discrete clouds, the middle section contains short streams, and the lower section contains long streams. Reference codes are as follows: T12 = Taylor et al. (2012), T13 = Taylor et al. (2013), K09 = Kent et al. (2009), K10 = Kent (2010), C07 = Chung et al. (2007), D07 = Duc et al. (2007), M07 = Minchin et al. (2007), G89 = Giovanelli & Haynes (1989), O05 = Oosterloo & van Gorkom (2005), K08 = Koopmann et al. (2008), S17 = Sorgho et al. (2017). The parent galaxy of VIRGOHI21 is believed to be NGC 4254 (VCC 307) while the Koopmann stream is associated with NGC 4534/DDO 137.

is strongly H I deficient, though the mass of H I in the plume can only account for about 10% of the missing gas. Both molecular and ionized gas were later detected in the stream, but both are an order-of-magnitude less massive than the H I (Verdugo et al. 2015). In contrast, NGC 4569 is strongly H I deficient but Boselli et al. (2016) find that 17%–42% of its missing H I can be explained by a phase change to (detected) H α . It is therefore unclear if phase changes can explain the lack of H I streams in the Virgo cluster.

In contrast, numerous ram pressure stripping simulations have shown that stripped H I can remain detectable at distances >100 kpc from its parent galaxy (e.g., Roediger & Brüggén 2008; Tonnesen & Bryan 2010). Cosmological simulations by Yun et al. (2019) found that 30% or more of gas-rich galaxies possess long one-sided gas tails, though this does not account for the phase of the gas. Other simulations have shown that while harassment cannot explain strong deficiencies, it can still produce easily detectable, long, one-sided H I streams (Duc & Bournaud 2008; Taylor et al. 2017).

Vollmer & Hutchmeier (2007) proposed that only the warm H I is stripped by ram pressure, quickly rendering it undetectable due to evaporation and dispersal. But this would still allow a 200 Myr detectability window, and some galaxies are so deficient that it appears that the cold, inner H I has also

been stripped. In short, none of the scenarios proposed are very satisfying solutions to the “missing stream” problem—at least in Virgo.

In this paper, we attempt to address these issues. Section 2 reviews the known optically dark H I features in Virgo. In Section 3, we attempt to quantify how many streams we expect to detect. In Section 4, we use new analysis techniques to search AGES data cubes again, uncovering a number of streams that were previously missed. We interpret the validity and physical nature of our detections in Section 5. Finally, in Section 6, we comment on these results and whether they alleviate the problems discussed above.

2. Known Optically Dark H I Features in Virgo

In order to quantify the (possible) discrepancy between the actual and expected number of H I streams in Virgo, we require a catalog of known features. We compile a catalog of optically dark H I features in Virgo with $v_{\text{hel}} < 3000$ km s⁻¹ from a literature search (see also Taylor et al. 2016 for more details), which is presented in Table 1.

We have arranged the features in Table 1 into three categories: isolated clouds, short streams attached to their parent galaxies, and much longer features. While most streams

Table 2
Galaxies with Known H I Streams, Comparing the Parent Galaxy H I
Deficiency with the Tail Mass

Name	M_{HIgalaxy} (M_{\odot})	H I deficiency	M_{HItail} (M_{\odot})	$\frac{M_{\text{HItail}}}{M_{\text{HImiss}}}$
VCC 1249	<8.2E6	∞	5.1E7	0.20
VCC 865	9.9E8	-0.05	7.0E7	...
VCC 497	1.5E9	0.63	9.0E7	0.02
VCC 465	1.6E9	0.20	2.0E8	0.22
VCC 1516	1.2E9	0.35	2.6E8	0.17
VCC 630	4.1E8	1.09	4.0E7	0.01
VCC 2066	2.0E8	0.88	9.0E8	0.69
VCC 979	1.9E8	1.26	5.4E7	0.01
VCC 1987	3.4E9	0.05	4.1E8	1.03
VCC 307	5.5E9	0.00	1.8E8	...
HI1225+01	1.6E9	-0.31	8.3E8	...
VCC 836	4.1E8	0.80	3.8E8	0.17

Note. We use the size and morphology parameters from GOLDMine to compute the expected H I mass, using the method of Solanes et al. (1996). Tail masses are taken from the references in Table 1. The missing mass is computed as the difference between the actual mass in the galaxy (ignoring the tail) and its expected mass. For VCC 1249, see Appendix A.11. VCC 307 (NGC 4254) is the likely parent galaxy of the VIRGOHI21 feature.

and clouds are typically less than 30 kpc in length, a handful are truly enormous, from 100 to 500 kpc in extent. Table 2 compares how the streams relate to their parent galaxies. The H I deficiency is quantified using the method of Haynes & Giovanelli (1984), using the parameters of Solanes et al. (1996, see their Table 2). The intrinsic scatter in the relation is generally taken to be around 0.3.

Of the 12 galaxies in Table 2, seven are significantly deficient while the others are non-deficient. The lack of correlation between deficiency and the presence of a stream is strengthened given that the vast majority of deficient galaxies in the cluster have no reported streams.

Table 2 also gives the ratio of the gas detected within a tail compared to the amount of gas lost according to the deficiency parameter ($M_{\text{HItail}}/M_{\text{HImiss}}$ column). The majority of tails are simple, linear, one-sided features, which contain much less than the amount of missing gas of their parent galaxies. This suggests that after gas removal, a rapid phase change or dispersal of the H I is necessary and sufficient to explain *most* of the features. This is a simple, appealing view of the evolution of the streams but there are two serious caveats. First, as discussed in T16, there are a small number of cases where the mass in the stream appears excessively large in relation to the parent galaxy. Second, it is unclear whether such a process is compatible with the presence of a few very long, massive streams: are those particular features somehow prevented from dissipating? We therefore need a way to predict how many galaxies should be actively losing gas and the conditions that can render the gas undetectable.

3. How Many Streams Do We Expect to Find?

There are three aspects to the problem: whether streams are observationally detectable, how many are currently forming, and the evolution of the streams as they disperse into the intracluster medium (ICM). In this section, we examine the first two aspects of observational limitations and stream formation rate. We will examine their evolution in Section 5.3.

3.1. Observational Restrictions

Almost all of the shorter streams in Table 1 are comparable in size to the Arecibo beam, or longer, and, thus, should be distinguishable from their progenitor galaxies even with the low-resolution Arecibo surveys. Furthermore, they are mostly quite massive, $\sim 10^8 M_{\odot}$. ALFALFA and AGES are both ostensibly far more sensitive than the VIVA survey: AGES reports a 1σ column density sensitivity limit of approximately $N_{\text{HI}} = 1.5 \times 10^{17} \text{ cm}^{-2}$ (at a line width of a single 10 km s^{-1} channel; Keenan et al. 2016); ALFALFA is about $5.0 \times 10^{17} \text{ cm}^{-2}$ (Grossi et al. 2008); VIVA is almost two orders of magnitude worse, at around $1.0 \times 10^{19} \text{ cm}^{-2}$ (Chung et al. 2009).

An important caveat is that column density is not necessarily a good sensitivity indicator. What the observations are actually sensitive to is the total mass within the beam. Gas can have an arbitrarily high value of N_{HI} , but if its mass is too small then the observations may not detect it (e.g., a dense but low-mass feature would have a low filling factor within a large telescope beam). Counterintuitively, a survey with a smaller beam and worse N_{HI} sensitivity may actually be more suitable for detecting low-mass features, provided that their N_{HI} is sufficient. This “beam dilution” is particularly important for single-dish telescopes, and interferometers are better adapted to detecting structures smaller than the beam scale.

With this in mind, we can compute the detectability of a stream if we make the idealized assumption that the stream is a linear, uniform-density cylinder. In this case, the signal-to-noise ratio (S/N) from a given survey will depend on the mass, length, velocity profile, and orientation of the stream with respect to the observer. Orientation has two effects, first on the projected length L_p :

$$L_p = L \sin(i) \quad (1)$$

where L is the intrinsic length of the stream and i is the inclination angle to the line of sight, such that $i = 0^\circ$ if the line of sight is parallel to the longest axis of the stream and 90° if perpendicular. The number of beams that the stream spans in projection will be given simply by L_p/B where B is the beam size. The stream can never (by definition) be smaller than a point source in any survey—it must always appear to span at least one beam. The form of the stream in observational data will be its true shape convolved with the telescope beam, but a reasonable approximation is given by:

$$N_{\text{beams}} = \max\left(1.0, \frac{L \sin(i)}{B}\right). \quad (2)$$

Second, orientation has a very similar effect on how many velocity channels the stream spans. Recall that the relevant parameter for detectability is the mass contained in each beam in each channel:

$$M = \frac{M_{\text{total}}}{N_{\text{beams}} N_{\text{chans}}}, \quad (3)$$

where M_{total} is the total mass of the entire stream. Given the standard equation for converting H I flux to mass:

$$M_{\text{HI}} = 2.36 \times 10^5 d^2 F_{\text{HI}}, \quad (4)$$

where for M_{HI} in solar units, F_{HI} is the total flux in Jy km s^{-1} , which for a single channel is given by $S/N \sigma_{\text{rms}} w$, where σ_{rms} is the rms noise level of the survey, w is the velocity width of

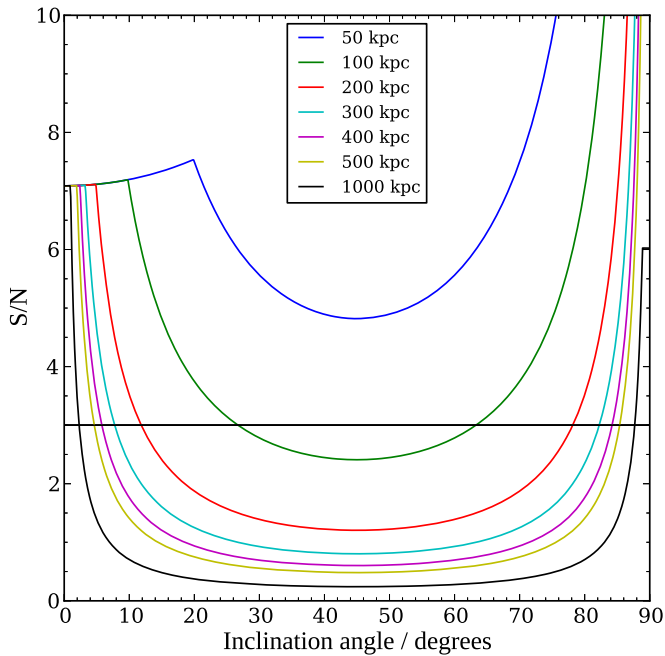


Figure 1. Expected S/N level of a linear stream of mass $M_{\text{H I}} = 1.45 \times 10^8 M_{\odot}$ and velocity width 500 km s^{-1} as a function of viewing angle, for various lengths, assuming survey capabilities equal to AGES (beam size of 17 kpc, rms of 0.6 mJy, and channel width 10 km s^{-1}). The black line shows a constant S/N level of 3.0, for reference. The vertical axis has been truncated, with an actual peak S/N > 100.0 . The “cut” at low inclination angles occurs when the stream spans less than one beam in projected length—a similar cut occurs at high angles when the stream spans less than 1 velocity channel.

the channel (in km s^{-1}), and d is the distance in Mpc. We can combine the above equations to calculate the S/N of a stream based on its intrinsic parameters and the survey’s capabilities:

$$S/N = \frac{M_{\text{total}}}{N_{\text{beams}} N_{\text{chans}} 2.36 \times 10^5 d^2 \sigma_{\text{rms}} w}. \quad (5)$$

If we disregard the cases where the stream is contained within a single beam or channel, then by Equation (2) and its velocity counterpart (we assume a velocity gradient of magnitude V along the longest axis of the stream), we can rewrite Equation (5) as

$$S/N = \frac{M_{\text{total}}}{\left(\frac{L}{B}\right) \sin(i) V \cos(i) 2.36 \times 10^5 d^2 \sigma_{\text{rms}}}. \quad (6)$$

Thus, while the noise level of the survey remains critical, the survey resolution only determines where the S/N is truncated (see below) but has no other influence over the curve. This may seem counterintuitive; for example, if one smooths data in velocity, the flux is spread into fewer velocity channels and so the S/N increases. Of course, this procedure also improves the σ_{rms} , and in practice, the resolution and σ_{rms} are not truly independent: to get the same σ_{rms} when the velocity resolution is higher requires a longer integration time.

Using Equation (6), we plot how S/N varies with inclination angle for a linear stream of given parameters (Figure 1). At low angles, flux is projected into a short spatial length, giving a high S/N despite a wide spread in velocity. At intermediate angles, the flux is spread out both in velocity and space, minimizing the S/N. At high angles, the S/N increases—

although it is now highly spatially extended, its projected velocity width is very small. For any given stream, there is a range of inclination angles within which it can be detected.

Perhaps more usefully, we can also consider the streams as a population. If we assume that the streams have a random orientation with respect to the observer, Equation (6) can be used to find the range of inclination angles at which a stream of any given parameters will be detectable—so giving the detectable fraction. The projected length of a stream should be at least two beams; otherwise, they will not be distinguishable from their parent galaxies.⁴ This means their detectable fraction never reaches 100%.

We do not know the properties of the entire population of streams in Virgo, but we do know about those that have been detected in VIVA. Assuming these are representative of the true stream population, then by this method, we can determine how many such features should be detectable to the ALFALFA and AGES surveys. Their median mass (see Table 1) is $1.45 \times 10^8 M_{\odot}$. We estimate their intrinsic lengths and velocity widths from the maximum observed values, 60 kpc and 110 km s^{-1} , respectively. The expected detection fraction is rather high, around 70% for both AGES and ALFALFA. The projected length is the limiting factor in this regime, not the total mass; hence, the identical spatial resolution of the surveys gives identical detection fractions.

The expected number of detected streams in any given survey depends on (1) the number of HI-detected galaxies in the survey region (439 for ALFALFA in the VCC region, 105 for AGES); (2) what fraction of those galaxies actually have streams, which we take to be 15% based on VIVA; (3) the geometrical correction for how many streams that exist should also be detectable, i.e., 70%. This gives expected stream numbers of 46 for ALFALFA and 11 for AGES. The actual numbers are five for ALFALFA and two for AGES. Hence, the geometric correction is insufficient to explain their low detected numbers. We now consider which galaxies are expected to be currently producing streams in the first place.

3.2. Stream Formation

The modeling of Köppen et al. (2018) provides an analytic model of ram pressure stripping. This considers how much pressure is required to strip the HI down to its observed radius (P_{req}) in comparison with an estimate of the local pressure the galaxy is actually experiencing (P_{loc}), given its position in the cluster. Given the uncertainties, a galaxy may be actively stripping if the ratio $P_{\text{loc}}/P_{\text{req}} \geq 0.5$. The main advantage to this is that it describes current stripping activity—potentially a much better proxy for the presence of a stream than HI deficiency. The disadvantage is that the necessary data are only available for a small fraction of the galaxies, so we cannot use it to predict the total number of expected streams in this region.

Despite this, the model can make more qualitative predictions. We do not expect every galaxy that is predicted to be an active stripper to have an HI tail, due to the distance uncertainty (which affects the calculated P_{req} value) and the possible geometrical dilution of the tail described in Section 3.1. If, however, ram pressure stripping is indeed the dominant gas-loss mechanism in the cluster, then we expect

⁴ Scott et al. (2018) discuss a search for spectral asymmetries. The effect is generally quite subtle but may prove fruitful for a future examination of the AGES and/or ALFALFA Virgo data.

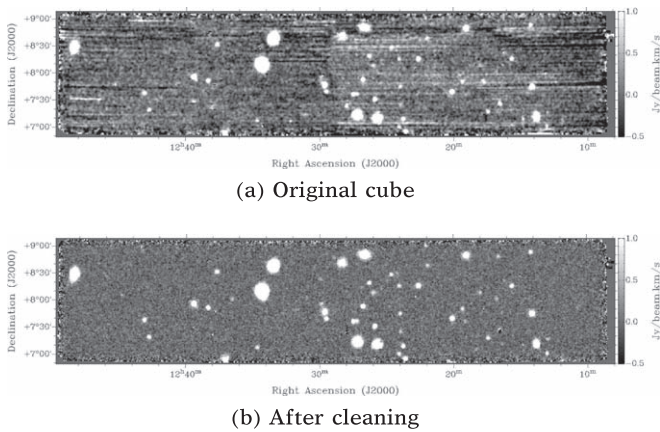


Figure 2. Moment 0 (integrated flux) maps of the AGES VC1 data cube, using the same velocity range ($100\text{--}3000\text{ km s}^{-1}$) and with the same color scale in both cases. The upper figure uses the standard data cube, which has no additional processing besides hanning smoothing; the lower figure uses the cleaning techniques described in Section 4. The rms of the spatial bandpass in the cleaned image is approximately 33% lower than in the raw image, whereas the mean pixel value is a factor of three lower in the cleaned image.

tails to be more common among galaxies with higher $P_{\text{loc}}/P_{\text{req}}$ ratios. We also expect every galaxy (with only rare exceptions due to harassment and ICM density variations) that has an H I tail to be an active stripper according to the model. We will return to this in Section 5.1.

4. Searching for Streams

4.1. Data Processing

We test the models of Section 3 using the two AGES Virgo data cubes described in Taylor et al. (2012, 2013). The much larger ALFALFA data set is not publically available, and the AGES data sets, though smaller, have the advantage of higher sensitivity. Both cubes are available via the AGES website at the following URL: <http://www.naic.edu/~ages/>.

There are two significant improvements to the data processing algorithms developed since the original analysis. The first is an implementation of the spatial bandpass processing algorithm MEDMED, described in Putman et al. (2002). AGES is an R.A.-parallel drift scan survey, with the baseline level of the spatial bandpass being nominally estimated as the median level of the entire scan. This is adequate for most scans in which galaxies occupy only a few percent of the bandpass; but where bright, extended sources are present, the baseline average value is overestimated. This results in “shadows” in the cube in R.A. (see Minchin et al. 2010). As in Taylor et al. (2014), we use a Python-based version of MEDMED that splits the scan into five boxes, measures the median of each, and then uses the median of the medians as the baseline. This almost completely eliminates the shadows, which would otherwise hamper the search for extended emission in the affected areas.

The second change, also described in Taylor et al. (2014), is to fit a second-order polynomial to the spectrum along each pixel in the cube. While the rms of each spectrum is not affected, the removal of the baseline variation from pixel to pixel greatly improves the “cleanliness” of the data, making it much easier to search for extended emission and improving the accuracy of flux measurements on extended structures. The combined effect of these cleaning processes is shown in Figure 2.

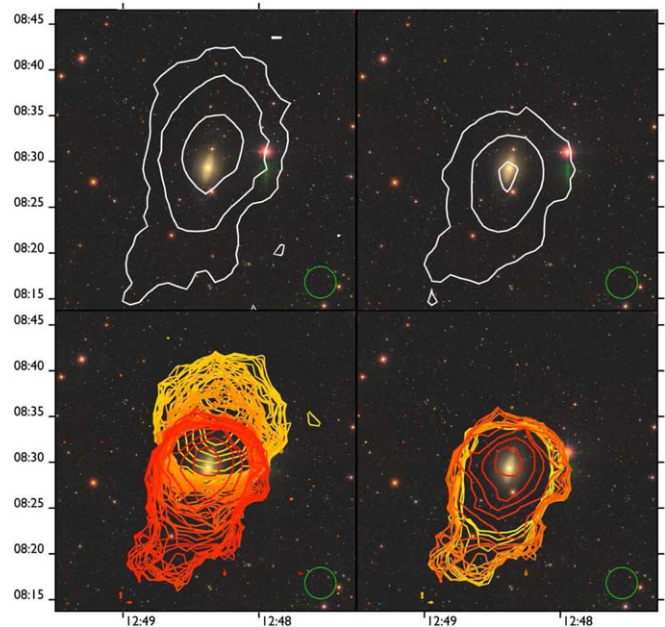


Figure 3. Different 2D display techniques for the same galaxy, VCC 2070. The background image is the Sloan Digital Sky Survey (SDSS) RGB image from the standard pipeline, the same in all panels. The top panels show moment 0 contours while the lower panels show renzograms. The left side images use the full velocity range of the galaxy while those on the right are restricted to the velocity range we identify as containing the associated stream. The green circle is the size of the Arecibo FWHM, $3/5$.

4.2. Search Technique

Another key development in our search for streams is the FITS viewer FRELLED, described in Taylor (2015). The main benefit here is the user can interactively create moment maps and contour plots, i.e., to find the most appropriate velocity and spatial range with which to examine each galaxy. We can also examine the data in 3D rather than conventional 2D slices, which can make visual identification of extended features much easier.

We found that the best way to detect extended emission was through inspection of renzograms (contour maps in which each velocity channel is represented by a different color; see Ruppen 1999) for noncircular features. Integrated flux maps, though of greater sensitivity to diffuse gas, tend to be problematic. The galaxies themselves often have marginally resolved gas disks—while the disks tend to have circular H I contours in every channel, their center is not quite at the same pixel position in each channel. Thus, integrating over the whole velocity range produces noncircular features that are not related to genuine extensions (see Figure 3).

Viewing renzograms in 3D shows essentially *isosurfaces* that display constant flux levels as a 3D surface rather than a 2D contour. This gives a powerful advantage in the search for noncircular extensions: since most channels tend to have circular contours, those with noncircular extended features easily stand out (especially if those features are coherent over several channels). Unlike volume renders, isosurfaces have the benefit of displaying the flux at an objective level that does not depend on viewing angle (see Taylor 2015 for a full discussion), and the 3D display makes it easier to see which channels possess extensions than the case of 2D renzograms (where the superposition of many channels can be confusing). We show an example in Figure 4.

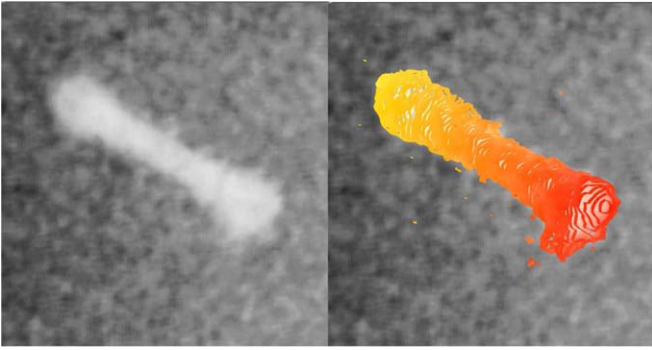


Figure 4. Example of using different visualization techniques to search for extended features. The left panel shows a volume rendering (integrating the flux along the line of sight) of VCC 2070 at an arbitrary angle. The extended gas tail is barely visible. The right panel shows the data cube rendered in exactly the same way but with a renzogram at 4σ overlaid. The extension at the low-velocity tip of the galaxy (right side of the image) is now much more obvious.

We limited our search to the velocity range $100 < v_{\text{hel}} < 3000 \text{ km s}^{-1}$, avoiding the Milky Way and high velocity clouds. We constructed renzograms/isosurfaces for every cataloged HI detection in this region, 106 out of our total of 108 Virgo detections for VC1 and VC2 combined. The two omissions were at such low redshifts that Milky Way contamination would make distinguishing any extended emission extremely difficult.

Our procedure was to begin with renzograms at 3σ and then increase the S/N level as appropriate. For the brightest sources, extensions are not visible at $3\text{--}5\sigma$ simply because the disk emission is very bright, “smearing” the emission into many pixels. Our requirement for a detection was that the noncircular features should be visible at a defined level per volumetric pixel (voxel) across a connected span of at least one beam (in addition to the galaxy’s disk) and over at least three channels. We cataloged possible streams by the noise level of the connected voxels as either certain ($>6\sigma$ per voxel), probable ($>4\text{--}6\sigma$ per voxel), or possible ($>3\text{--}4\sigma$ per voxel). We discuss these levels in detail in Section 4.5.

Maps of the individual certain or probable detections are shown in Figure 5. We do not discuss the less-confident detections here but present them in the Appendix. The full catalog of the stream status of all of the galaxies in this region (excluding those with no streams of any kind) is shown in Table 3.

We cataloged four streams as certain, six as probable, and 16 as possible. We also found eight galaxies with HI contours with no indications of asymmetry but that had a distinctly “noisy” appearance, sometimes even at the 7σ level. None of the remaining 73 galaxies showed any indications of any unusual HI features, though 20 of these were of rather low S/N (<10), so extensions would be difficult to detect.

4.3. Measuring the Streams

Unlike the galaxies in Taylor et al. (2014), the Virgo objects are marginally resolved and, thus, cannot be measured as point sources and subtracted to allow objective measurements. This means we are compelled to resort to more subjective procedures. We use FRELLED’s capability to define volumes of arbitrary shape and sum the flux within them, manually defining volumes that we believe only contain flux from the extended HI. Thus, the estimates of the stream masses in

Table 3 should be treated with caution (the estimated ratios $MHI_{\text{stream}}/MHI_{\text{miss}}$ are similar to the values for the Chung et al. 2007 sample, as in Table 2, though on the low side). We do not attempt this procedure at all for galaxies with noisy contours.

We measure the length of the streams as the distance from the center of the galaxy to the most distant extension of the stream contours. We do not apply the correction for beam smearing described in Wang et al. (2016) as the difference is only a few kpc for our sources, and our errors are dominated by the problems of determining the edge of the parent galaxy’s disk. Additionally, the beam size means that we cannot accurately measure the thickness of the streams—the apparent visual difference in thickness of the streams compared to their parent galaxies simply reflects the relative brightness of stream and galaxy, not their dimensions.

4.4. Comparisons to Other Data

Six galaxies in our sample have interferometric observations. VCC 2070 and VCC 1555 were observed with VIVA, with shorter extensions detected at similar orientations to those detected here (see Figures 11.1 and 11.3). The tail of VCC 2066/2062 has a very similar overall morphology in both AGES and the VLA observations of Duc et al. (2007), though the VLA data shows structures within the tail that AGES cannot resolve. The morphology of the gas cloud close to VCC 1249 is very similar in AGES (see T12 Figure 21) to the KAT7 observations of Sorgho et al. (2017, hereafter S17; see their Figure A1.3). In general, the AGES data support the existing interferometric observations, in some cases extending the length of the tails significantly.

There are two exceptions. One is VCC 1205 (see Appendix A.10), the extension of which is not described by S17. However, this is not surprising—their observations are nominally five times less sensitive than ours, with a 1σ column density sensitivity of $8 \times 10^{17} \text{ cm}^{-2}$. This is reduced further at the position of VCC 1205 as that region was only observed with KAT7. Additionally, S17 only detect a small part of the ALFALFA Virgo 7 cloud complex described in Kent et al. (2009; which similarly happens to be at the edge of the field where only KAT7 data was taken), and the authors attribute this to the gas being at a low column density and below the sensitivity of the interferometer.

More puzzlingly, the feature described in S17 associated with AGESVC1 293 is not visible in the AGES data. Here, the KAT7 and WSRT pointings overlap, though the galaxy is near the edge of the survey fields where sensitivity is again somewhat reduced (see S17 Figure 3). It has an HI mass of $2.0 \times 10^7 M_{\odot}$ and a W50 of 87 km s^{-1} . The morphology of the source is irregular, so beam dilution may play some role, but the main feature is comparable in size to the Arecibo beam. If entirely contained within the Arecibo beam, the average column density in each 10 kms AGES velocity channel would be $1.2 \times 10^{18} \text{ cm}^{-2}$, well above the AGES sensitivity limit. Deeper observations are needed to confirm the existence of this source.

4.5. Estimating the False Detection Rate

Our criteria for “probable” detections being at least 4σ may seem weak, implying that we could expect a high fraction of our results to be spurious. In this section, we examine this

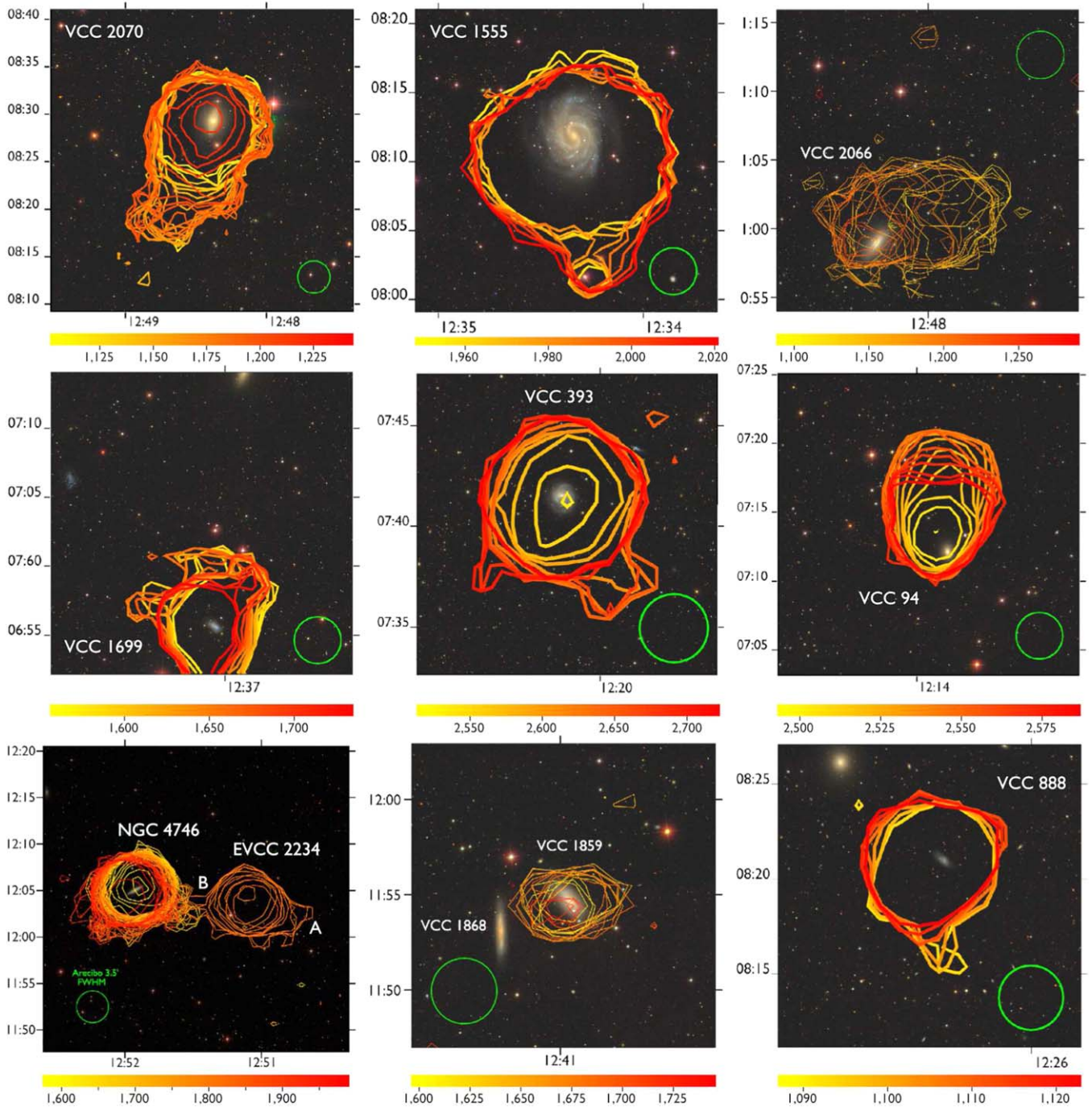


Figure 5. Renzograms of the “certain” (VCC 2070, VCC 1555, and VCC 2066 on the top row; EVCC 2234 is in the bottom left panel) and “probable” stream detections. The contour levels are of fixed value, with color indicating the channel. The S/N level of the contour (typically 4σ , equivalent to a column density of $N_{\text{H I}} = 6 \times 10^{17} \text{ cm}^{-2}$) and velocity range of the renzogram (shown by the color bars in units of km s^{-1}) have been manually adjusted in each case to reveal the streams most clearly, so they do not always show the full velocity range of each galaxy—for exact individual values, consult the [Appendix](#). The green circles show the Arecibo beam size.

statistically by three different methods. Throughout, it is crucial to remember that our criteria for identification rely not just on S/N but also on the spatial and velocity extent of the features.

4.5.1. The Number of Similar Features in Galaxy-free Regions of the Data

If the claimed streams are actually just fluctuations in the noise, then they should be present throughout the entirety of the data cube. Although difficult to disentangle from bright,

marginally resolved galaxies, in empty regions, it is straightforward to find and measure such features using objective, repeatable procedures.

We begin by masking the galaxies and the identified streams, which accounts for about 5% of the total volume of the VCI data cube. For the remaining pixels, we use the STILTS package (Taylor 2006) to match groups of connected pixels at or above a range of S/N levels. We then quantify the number of groups of pixels based on both the number of connected pixels and the S/N level. Given the detection rate in the galaxy-free regions

Table 3
Catalog of All of the Extended H I Features Detected in AGES in the Virgo Cluster

AGES ID	Galaxy ID	Galaxy $M_{\text{H I}}$ (M_{\odot})	Missing $M_{\text{H I}}$ (M_{\odot})	Stream Code	$\frac{P_{\text{loc}}}{P_{\text{req}}}$	Stream Length (kpc)	Stream $M_{\text{H I}}$ (M_{\odot})	$\frac{M_{\text{H I stream}}}{M_{\text{H I miss}}}$
AGESVC1 269	VCC 1555/NGC 4535	1.1E9	3.0E9	0	0.87	60	3.4E8	0.113
AGESVC1 270	VCC 2070/NGC 4698	1.2E9	4.3E9	0	0.21	75	2.1E8	0.049
AGESVC2 025	EVCC 2234	1.0E8	1.7E8	0	...	34	5.4E6	0.032
AGESVC2 020	VCC 2066/NGC 4694	2.5E8	1.3E9	0	0.17	50	9.0E8	0.692
AGESVC1 256	VCC 1699	5.3E8	6.0E7	1	2.33	32	3.4E7	0.567
AGESVC1 202	VCC 94/NGC 4191	1.7E9	-3.7E8	1	...	98	1.5E8	-0.405
AGESVC1 246	VCC 888	2.4E8	7.7E8	1	...	35	2.9E6	0.004
AGESVC1 210	VCC 393/NGC 4726	5.3E8	1.4E9	1	...	65	2.0E7	0.014
AGESVC2 022	VCC 1972/NGC 4647	4.1E8	6.3E8	1	0.30	51	1.7E7	0.027
AGESVC2 033	VCC 1859/NGC 4606	4.5E7	2.8E9	1	0.01	17	5.2E7	0.002
AGESVC1 229	VCC 667	2.9E8	2.7E9	2	...	42	3.0E7	0.011
AGESVC1 204	None	3.6E8	3.5E8	2	...	46	1.6E7	0.046
AGESVC1 207	VCC 199/NGC 4224	8.3E8	4.1E9	2	...	49	3.0E7	0.007
AGESVC1 232	None	8.2E7	1.0E8	2	...	33	2.5E6	0.025
AGESVC1 278	VCC 1011	1.7E8	7.1E8	2	0.23	37	3.0E6	0.004
AGESVC1 238	VCC 688/NGC 4353	1.5E8	1.3E9	2	...	23	1.2E7	0.009
AGESVC1 284	VCC 740	1.9E8	3.8E8	2	...	42	1.1E7	0.029
AGESVC1 248	VCC 713/NGC 4356	8.9E7	6.5E9	2	...	66	3.9E7	0.006
AGESVC1 272	VCC 1725	1.3E8	5.0E8	2	0.40	36	4.3E6	0.009
GLADOS 001	None	6.5E7	2.1E8	2	...	46	1.1E7	0.052
AGESVC1 286	VCC 514	1.2E8	1.9E9	2	...	40	6.5E6	0.003
AGESVC1 235	None	2.6E7	7.1E7	2	...	59	5.7E6	0.080
AGESVC2 063	None	1.5E7	4.5E7	2	...	17	1.0E6	0.022
AGESVC2 018	VCC 1868/NGC 4607	2.5E8	1.0E9	2	0.25	40	1.9E7	0.019
AGESVC2 027	NGC 4746	8.3E8	1.8E9	2	...	34	5.8E7	0.032
AGESVC2 025B	EVCC 2234	1.0E8	1.7E8	2	...	34	8.1E6	0.048
AGESVC1 259	VCC1952	1.4E8	3.8E8	3	...	36
AGESVC1 212	VCC1205/NGC 4470	4.7E8	9.4E8	3	0.52	39
AGESVC1 261	VCC1394	2.5E7	...	3	...	32
AGESVC1 225	VCC1791	4.5E8	3.7E8	3	...	59
AGESVC1 281	VCC1249	5.1E7	...	3	...	40
AGESVC1 244	VCC566	4.1E8	-8.5E7	3	...	47
AGESVC1 220	VCC318	2.1E9	6.1E8	3	...	81
AGESVC1 216	VCC207	1.5E8	2.0E8	3	...	34
AGESVC1 268	VCC 2007	2.5E7	1.3E8	4	0.02
AGESVC1 240	VCC 938/NGC 4416	2.6E8	6.5E8	4	0.05
AGESVC1 292	VCC 1575	9.0E7	6.9E8	4	0.06
AGESVC1 279	VCC 1193/NGC 4466	1.7E8	1.5E8	4	0.10
AGESVC1 263	VCC 1758	2.0E8	3.9E8	4	0.16
AGESVC2 019	VCC 1955/NGC 4641	3.7E7	4.0E8	4	0.18

Note. All measurements are derived from AGES data except for those of AGESVC2 020 (VCC 2066)—as this is on the southern limit of the data where measurements may not be accurate, we use the values from Duc et al. (2007) instead. The sections divide the table according to stream type, where 0–2 denote possible streams (0 means the detection is certain, 1 probable, and 2 possible), and 3 indicates that the galaxy has noisy contours with no preferred direction for the extensions. For completeness, we also show category 4, meaning no detected streams, for those objects where the pressure ratio described in Section 3.2 was calculated.

and the total volume searched for extensions, we can estimate the number of false detections we expect around the galaxies. The results are shown in Figure 6.

At 4σ per voxel, even groups of only five connected pixels (approximately one beam in one channel) are expected to be so rare that they are unlikely to cause significant contamination. Five pixels is extremely small—10 is more reasonable for our “probable” and “certain” detections, which generally fill at least one beam and are found in three or more channels. With 10 or more pixels, streams can be considered reliable even at 3.5σ . Furthermore, the curves plotted in Figure 6 will significantly

overpredict the number of false detections: this figure assumes that a spurious clump found at any location within the searched volume would be mistaken for an extension. In reality, the clump would have to appear in a very specific, much smaller region—if it coincided with a galaxy, it would not be visible at all, whereas if it was too far from the galaxy, it would be identified as an independent object rather than an extension. We conclude that our “certain” and “probable” identifications suffer a negligible rate of false positives, though doubtless there may be contamination in our “possible” features. It should be remembered that only 36% of the galaxies inspected in the

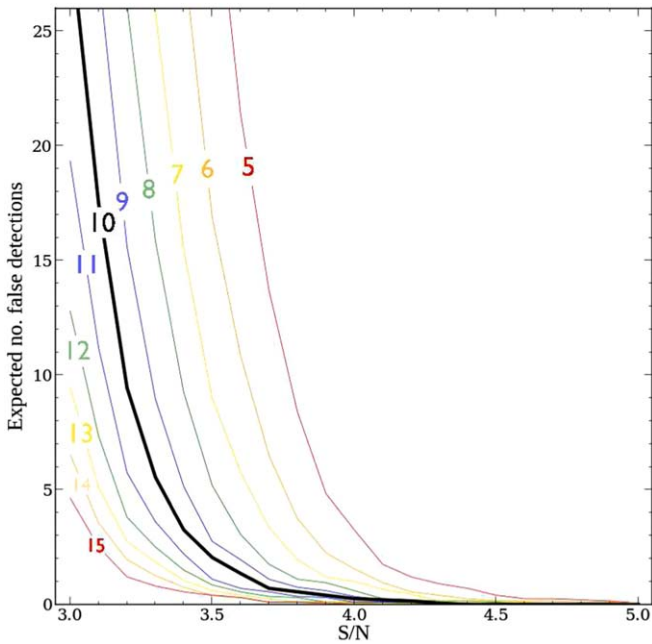


Figure 6. Expected number of false detections of streams at different S/N levels (x-axis) and number of connected pixels (annotations). This is based on a search of the empty regions of the the VC1 data cube, described in the text. The y-axis value has been scaled according to the volume spanned by the galaxies and their streams and been truncated at 26 (the total number of certain, probable, and possible streams).

VC1 cube showed any signs of extensions at all—even the most modest potential streams included in our catalog are notably different from most of the galaxies in the data.

4.5.2. Searching for Simulated Streams of Known Parameters

Using artificial galaxies and streams with real noise, we can also test our subjective search techniques. In this way, we can examine (a) whether the noise will allow us to detect features as weak as those we claim to have detected and (b) whether we would visually identify more false positives than the objective procedure suggests.

We create an artificial galaxy with parameters ($S/N = 55.0$ and velocity width of 220 km s^{-1}) based on the median values of the galaxies we have identified as having sure or probable streams. For the galaxy, we use either a simple point source or a more realistic model based on the radially averaged profile of the real, marginally resolved VCC 975. We create a stream beginning with a grid of 6×2 pixels of a uniform S/N level ($3, 4$ or 5σ), which we then convolve with a $3/5$ Gaussian. This we then add to either the first one, two, or three consecutive channels in the artificial galaxy data set, our aim being to explore the detectability of the weakest features.

Next, we run a Python script that chooses random pixels within the masked VC1 cube and checks for the presence of masked pixels within the appropriate surrounding volume. If any are found, another pixel is chosen, and this is repeated until a suitable region is found. We then add the galaxy and stream into this region of pure noise. The data in this region is extracted, and the procedure is repeated 100 times to create galaxies+stream+noise data cubes. The properties of the galaxy and stream do not vary, so this procedure tests only the influence of the noise. An example subset of the data is shown in Figure 7, plotting renzograms of the point-source

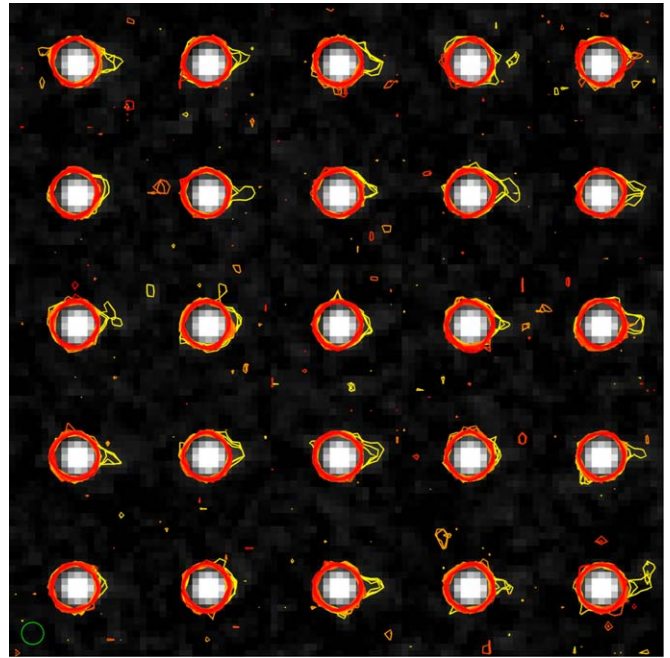


Figure 7. Example subset of artificial galaxies with extensions combined with real noise from the AGES VC1 data cube. In this case, the extension has an original S/N level of 3σ (boosted slightly by the presence of the galaxy) with the contour at 3.5σ . This approximately corresponds to some of our faintest claimed detections. When visible, the extension is usually clear, whereas there are almost no visible false positives even at this low S/N level.

case, with the stream extending from the center of the galaxy to the right.

We inspect the final data set visually, varying the contour level from 3.0 to 5.0σ in steps of 0.5 . At each level, we record how many galaxies show clear signs of the artificial stream in their renzograms. We require a detection to span at least one beam, the same number of channels as it was injected in, and be present at the correct location. We also count the number of galaxies with similar features that are not at the correct location, i.e., false positives. Knowing the size and orientation of the stream makes this process very fast, enabling us to explore a large parameter space of detectability (note that the detection criteria deliberately probe very low S/N levels and channel numbers, and do not reproduce the criteria used in the actual search).

The results are shown in Figure 8. Since the streams are added to a bright galaxy, their final S/N is usually slightly higher than their initial value; hence, it is sometimes possible to detect nominally faint streams at surprisingly high S/N values. “Completeness” here is in the usual sense, i.e., the fraction of known streams that were detected. We cannot properly measure reliability here, as this depends on the number of injected streams, which is a free parameter in this exercise. Instead, the independent parameter is the number of false positives.

We find that at very low S/N levels, the data is essentially one contiguous set of pixels from which nothing whatsoever can be discerned. At high S/N levels, one sees only the bright galaxies. In between these extremes, there does not exist a realm in which one sees significant numbers of features resembling the streams we see around actual galaxies. Such features do exist but are always rare and, hence, unlikely to be found in locations where they would be mistaken for streams.

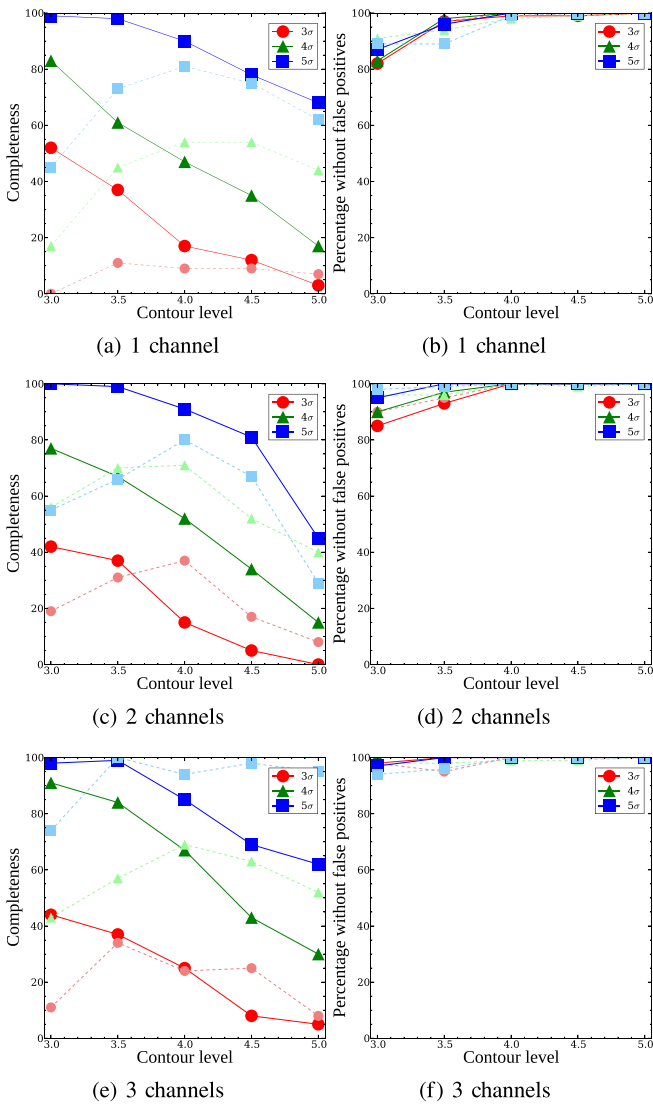


Figure 8. Completeness levels (left) and false-positive rate as a function of contour level for sources injected into different numbers of channels (1, 2, and 3 from top to bottom). The line color indicates the original S/N level of the injected source. The solid lines show the case of using a point source for the galaxy while dashed lines use a more realistic galaxy profile.

Essentially, the noise can obscure real extensions, but it does not create many spurious features.

4.5.3. A Blind Search for Simulated Streams of Unknown Parameters

An even more realistic approach is to vary the properties of the streams so that we do not know if a stream is even present at all. We modify the injected streams to randomly vary their: (i) direction, so that they are assigned to one of eight different directions (N, NE, E, etc.); (ii) length, ranging from 6 to 8 pixels (we found that below 6 pixels, the streams are not recoverable due to the large apparent size of the simulated galaxy); (iii) S/N, ranging from 3.0 to 5.0; and (iv) number of channels, from zero through five, inclusive so that some streams are not actually injected at all. We also vary the absolute value of the channels used so that the colors of the renzogram provide no information of the presence of a stream. Tests showed that the weakest stream in this parameter space was at the very limit of visual detectability, whereas the strongest is extremely obvious.

Here, we do not impose the strict requirements on any potential detections as in Section 4.5.2 but simply try to decide if there is anything present that we might classify as a detection. We allow ourselves to vary the contour level but do not demand that any particular level is necessary—we attempt to select on the same basis as we did for the actual search. This is considerably slower than in Section 4.5.2 but is far more realistic. As before, we injected 100 potential streams (including those spanning zero channels) into real AGES noise.

Due to the random number of channels selected, a total of 76 streams were actually injected. We recovered 56 of these, giving a completeness of 74%. We also recorded five false positives. All of these were weak compared to the real sources: the strongest being 4σ in two channels, which is fainter than any of the real streams identified as “sure” or “probable.” Thus, it seems extremely unlikely that any of our “sure” and “probable” features identified in the real cluster are due to noise: the overwhelming probability is that they are real, physical structures. Again, we emphasize that the reliability level of the “possible” detections is surely lower.

5. Interpreting the Streams

5.1. Comparison with the Stripping Predictions

As described in Section 3.2, the advantage of the Köppen et al. (2018) model over HI deficiency is that it directly describes current stripping activity. While it is difficult to predefine an exact value of the ratio $P_{\text{loc}}/P_{\text{req}}$ to distinguish active from past strippers, the broader predictions of the model are borne out reasonably well. Of the galaxies with streams of all levels of confidence or noisy contours (11 objects), the median $P_{\text{loc}}/P_{\text{req}}$ ratio is 0.28. Examination of Table 3 suggests that a $P_{\text{loc}}/P_{\text{req}}$ ratio of 0.2 is a plausible (though rough) value to distinguish active from past strippers. Using this in the model, we can state that of the 10 galaxies with detected tails, eight should be actively losing gas and two should be past strippers; of the nine galaxies without tails, six are predicted to be passive and three should be active strippers. This broadly supports the assumption that the bulk of the streams should be produced by ram pressure stripping.

While we lack the advantages of resolution from interferometric studies, we can still measure all of the same major properties: morphology (at least to say whether a tail is one-sided), length, kinematics, and mass. In our view, all of these tend to support the ram-pressure origin scenario of the tails. They are mostly one-sided, the brightest emission occurs over a relatively short velocity range corresponding to that of the parent galaxy (as in the tails in Chung et al. 2007), and they are of comparable length to the Chung et al. (2007) tails, though they are of somewhat lower mass.

5.2. Alternative Explanations

HI asymmetries can be produced by internal and external processes. Tidal structures in Virgo (e.g., Minchin et al. 2007; Koopmann et al. 2008) are usually longer and show more complex, haphazard structures and kinematics, which are also seen in numerical simulations (e.g., Taylor et al. 2017). Other external processes, such as mergers and accretion, have been invoked in other environments (Noordermeer et al. 2005; Portas et al. 2011), but neither of these is likely in the high-velocity dispersion of a cluster.

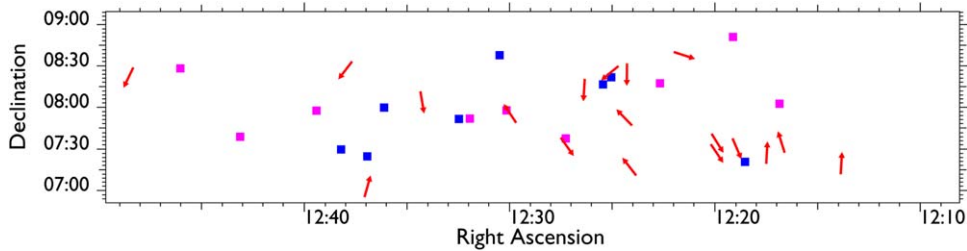


Figure 9. Map of all of the stream candidates in the VC1 region. The red arrows show the direction that the streams point away from their parent galaxies. The blue squares are clouds with no optical counterparts, and the magenta squares are galaxies with noisy contours but no clear linear extension.

Could such asymmetrical features be due to internal processes? Unfortunately, comparable studies of isolated galaxies are very rare (three isolated galaxies were targeted with AGES, none of which show extensions—see Minchin et al. 2016). Even then, the authors can seldom (if ever) rule out external processes (e.g., Pisano et al. 2002) and sometimes even find that this is the most likely explanation despite the isolation (Ramírez-Moreta et al. 2018). There are few catalogs of isolated galaxies with resolved HI maps, but those that exist broadly suggest that features as long and one-sided as those in the present work are far more likely to result from environmental effects. Noordermeer et al. (2005) note that only 7% of isolated galaxies are even “mildly” asymmetric. Espada et al. (2011), using unresolved line profiles, find that the rate of asymmetry is very low in isolation (2%) compared to the denser field environment (10%–20%). Pisano et al. (2002) describe a VLA survey of 41 isolated galaxies, of which just two (NGC 895 and IC 5078) have clear optically dark HI extensions. The extension of NGC 895 is morphologically very different to the tails described here, while the authors propose that mergers are responsible for the features in IC 5078. Scott et al. (2014) detect an extension 12 kpc in length, but even for this relatively short feature, the authors believe the cause is an external satellite.

In short, while asymmetric extensions are very common in group environments, they are rare in isolation (though there is a lack of large catalogs to properly quantify this). The only features comparable in both length and morphology to those we have described here are widely attributed to various environmental mechanisms, and we can find no evidence in the literature for internal causes.

5.3. The Evolution of the Streams

Using the Köppen et al. (2018) model, and assuming radial infall, we can estimate the point at which the ram pressure becomes sufficient to start removing gas from the galaxy. We assume this occurs when the ratio $P_{\text{loc}}/P_{\text{req}} \geq 0.5$. We can then derive the time of flight from this point to the galaxy’s current cluster-centric position, allowing us to calculate the dissolution rate. We find rates of typically $1\text{--}10 M_{\odot} \text{ yr}^{-1}$, with the time since stripping beginning around 200 Myr. Very similar rates are obtained by the objects described in Chung et al. (2007). If these are correct, then the detectable lifetime of the streams is highly variable (simply because of their mass), from a few megayears to a few gigayears. Similar survival times have been calculated independently by Kent et al. (2009) and Boselli et al. (2018). The least-massive streams are likely in a state of active replenishment; otherwise, their lifetime would be so short that we would not expect to detect them, whereas the most massive

streams can survive long after the stripping event by virtue of their high mass.

5.4. Relation to the Dark Clouds

Figure 9 shows that three of the dark clouds appear to be aligned with two of the streams. In one case (GLADOS 001/AGESVC1 231), the alignment is likely just a projection effect, as the velocity difference between the two is over 700 km s^{-1} . In the other case (VCC 740/AGESVC1 247 and 282), the velocity difference between the stream and the clouds is small; however, the stream is rather weak. The conclusion of T16 and Taylor et al. (2017) that the clouds are unlikely to be the result of gas stripping appears to be sound.

The dissolution rates calculated in Section 5.3 imply that we are witnessing the clouds in the final few Myr of their existence (given their low masses). This is a similar lifetime calculated as in Taylor et al. (2016, 2017) and considerably shorter than the ~ 100 Myr timescales estimated in Taylor et al. (2018). A caveat is that these rates might strongly vary depending on the density of the objects (i.e., allowing them to self-shield from ionizing radiation would reduce evaporation as well as give them stronger self-gravity), of which we, at present, do not have direct measurements.

5.5. Galaxies with Noisy Contours

Figure 10 provides a comparison of galaxies with smooth and irregular contours. It is possible that in the weaker cases, some of these irregular features are not real, but some cases, which are seen at 5σ in many pixels and channels, are unambiguous. These galaxies show no obvious coherent distribution within the cluster (Figure 9). One possibility is that they are actively losing gas but with motion mainly along the line of sight. Another is that they are losing gas by different, internal mechanisms, e.g., that the extensions are only due to temporary gas displacement (not complete ejection) via supernovae; for example, many dwarf galaxies show irregular contours (Swaters et al. 2002). While mergers are not expected in the cluster environment, IC 5078 in Pisano et al. (2002, see their Figure 40) shows intriguingly similar contours to these “noisy” galaxies, which the authors attribute to a possible minor merger.

6. Summary and Discussion

While approximately 60% of the late-type galaxies in Virgo show significant HI deficiencies, only 2% have previously documented streams. We might expect to see more galaxies in the process of actively losing gas, but quantification is difficult as many different factors influence the exact number of expected streams: how many galaxies are currently stripping,

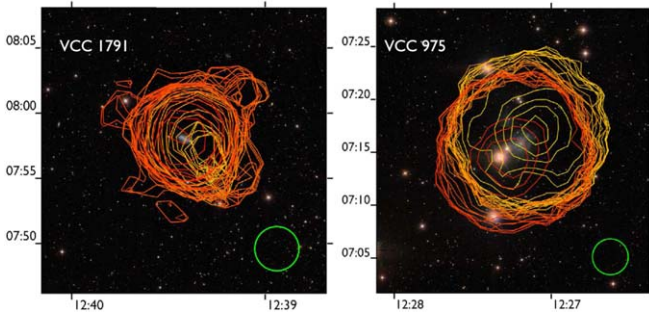


Figure 10. Example renzograms of a galaxy identified to have unusually noisy contours (AGESVC1 225, left) compared with another deemed to have clean contours (AGESVC1 277, right). The S/N level of the contours is 5.0 in both cases. Both are bright sources with peak S/N levels of 113 for AGESVC1 225 and 130 for AGESVC1 277. Note that since both sources are marginally resolved, a slight position shift in the center of their contours can be seen, especially for VCC 975.

the detectability of the streams in HI surveys given the stream geometry, orientation and kinematics, and the gas phase change rate.

We found through a geometric model that the orientation of the streams is unlikely to significantly reduce the detected number, assuming that previous detections are representative of the full population. Based on existing detections and the geometrical correction, we estimated that ALFALFA should detect 46 streams and AGES 11. Additionally, the model of Köppen et al. (2018) predicts that streams should tend to be associated with galaxies of higher $P_{\text{loc}}/P_{\text{req}}$ (the ratio of predicted local ram pressure and required pressure to explain the observed HI deficiency), and while not every galaxy with a high pressure ratio should have a tail, most galaxies with tails should have high ratios.

We re-examined the two AGES Virgo cubes using upgraded data processing and visualization techniques. We found a minimum of 10 streams (only one of which was previously known) and potentially as many as 26. This included galaxies observed in VIVA for which only much shorter tails were previously seen, suggesting that our higher detection rate is in part due to the greater sensitivity of AGES. We demonstrated using statistical analyses that our 10 most confident detections are too bright, extended and coherent to be a result of noise. The predictions from the Köppen et al. (2018) model appear to hold true. Furthermore, we can make a quantitative prediction for future surveys that streams will be most commonly associated with galaxies with $P_{\text{loc}}/P_{\text{req}} \gtrsim 0.2$.

Several factors have contributed to the puzzling lack of previous stream detections, most notably, quantitative estimates of: (1) the number of currently active stripping galaxies; (2) the time that galaxies have spent thus far in the cluster; (3) the evaporation and dispersal rate of stripped material; and additionally, (4) the discovery of previously unknown streams. While a naive comparison of the number of deficient galaxies and those with streams shows a clear mismatch, the more detailed analysis reveals a much better agreement.

While a few Virgo cluster streams contain a significant fraction of the missing gas, most contain only a few percent of the missing gas mass of their parent galaxy (in contrast, streams in other environments often contain an appreciable fraction of the HI mass of the parent, as discussed in Taylor et al. 2014). This strongly suggests that in most cases, a phase change occurs during the stripping process that renders much of the

stream undetectable to HI surveys. There is supporting evidence for this in other clusters: Gavazzi et al. (2018) find that 50%–60% of the observed late-type galaxies in the Coma cluster have H α tails.

The Köppen et al. (2018) model allows a prediction of the time each galaxy has been undergoing active stripping. For the galaxies with streams, this allows us to estimate the dissolution time independently of the physical processes at work, which are typically $1\text{--}10 M_{\odot} \text{ yr}^{-1}$. In combination with the time spent within the cluster thus far, these rapid dissolution rates are consistent with the existence of both a few long, relatively massive streams and a larger population of shorter, less-massive tails. Massive streams can persist for longer due to their greater mass, whereas less-massive streams are only detectable due to constant replenishment, as material is still being stripped from their parent galaxy. The dissolution rates also suggest that, if the optically dark isolated clouds are of a similar nature to the streams, we must be witnessing them in a very short detection window, and they should disappear in the next few Myr.

We expect to detect a similar number of streams with WAVES, which has a similar sensitivity and area of coverage to the AGES Virgo fields (Minchin et al. 2019). Better statistics will allow for further tests of the stream models and place more constraints on the nature of the optically dark clouds, but our information about the features described here is limited by the resolution of Arecibo. Future observations at comparable column density sensitivity and higher resolution may give much more precise information on the nature and formation mechanism of individual streams.

We are grateful to the anonymous referee whose comments improved the manuscript.

This work was supported by the Czech Ministry of Education, Youth and Sports from the large Infrastructures for Research, Experimental Development and Innovations project LM 2015067, the Czech Science Foundation grant CSF 19-18647S, and the institutional project RVO 67985815.

This work is based on observations collected at Arecibo Observatory. The Arecibo Observatory is operated by SRI International under a cooperative agreement with the National Science Foundation (AST-1100968), and in alliance with Ana G. Méndez-Universidad Metropolitana, and the Universities Space Research Association.

The SOFIA Science Center is operated by the Universities Space Research Association under NASA contract NNA17BF53C.

This research has made use of the GOLDMine Database. This research has made use of the NASA/IPAC Extragalactic Database (NED), which is operated by the Jet Propulsion Laboratory, California Institute of Technology, under contract with the National Aeronautics and Space Administration.

This work has made use of the SDSS. Funding for the SDSS and SDSS-II has been provided by the Alfred P. Sloan Foundation, the Participating Institutions, the National Science Foundation, the U.S. Department of Energy, the National Aeronautics and Space Administration, the Japanese Monbukagakusho, the Max Planck Society, and the Higher Education Funding Council for England. The SDSS website is <http://www.sdss.org/>.

The SDSS is managed by the Astrophysical Research Consortium for the Participating Institutions. The Participating

Institutions are the American Museum of Natural History, Astrophysical Institute Potsdam, University of Basel, University of Cambridge, Case Western Reserve University, University of Chicago, Drexel University, Fermilab, the Institute for Advanced Study, the Japan Participation Group, Johns Hopkins University, the Joint Institute for Nuclear Astrophysics, the Kavli Institute for Particle Astrophysics and Cosmology, the Korean Scientist Group, the Chinese Academy of Sciences (LAMOST), Los Alamos National Laboratory, the Max-Planck-Institute for Astronomy (MPIA), the Max-Planck-Institute for Astrophysics (MPA), New Mexico State University, Ohio State University, University of Pittsburgh, University of Portsmouth, Princeton University, the United States Naval Observatory, and the University of Washington.

Appendix Comments on Individual Streams

In this section, we describe the individual streams in more detail. We also provide figures of each stream not given in the main text (for those not shown here, see Figures 5, 10, and 11.1–11.18). All figures are renzograms unless otherwise stated, with nearby galaxies labeled and the target galaxy unlabeled in the center of the figure. We also give the contour level shown in the renzogram (for reference, 1σ is equivalent to $N_{\text{HI}} = 1.5 \times 10^{17} \text{ cm}^{-2}$) for each galaxy figure and the exact velocity range used for each renzogram.

A.1. VCC 2070

This is our clearest detection of a stream and perhaps the most surprising. The galaxy is near the edge of cube and about 1.7 Mpc in projection from M87. The edge of the stream (at 4σ) reaches four Arecibo beams from the center of the galaxy, giving it a maximum extent of about 70 kpc. The stream is visible in at least 12 velocity channels and peaks at around 8σ above the noise. This galaxy is one of only two in the VC1 area observed with VIVA. Although the long stream is not detected, the VIVA moment 0 map clearly shows a ragged edge (with a hint of a short extension) on the same side of the galaxy as the long AGES stream, with the opposite edge being much smoother—see Figure 11.1.

This detection clearly demonstrates the capacity of the AGES observations to detect features not visible to VIVA because of its comparatively poor column density sensitivity, bearing in mind the caveats discussed in Section 3.1. The main reason this stream appears to have been missed in our original search is probably beam smearing—as shown in Figure 4, the stream appears to be obvious *only* if the data is processed in the correct way, with the use of contour maps greatly enhancing the noncircular HI extension.

This galaxy is shown in Figure 5 with the contour at 4σ over the velocity range 1102–1242 km s^{-1} .

A.2. VCC 1555

This is our second unambiguous detection of a stream. It appears in Figure 5 (and in the data cube) almost to resemble a companion galaxy, but we can find no optical counterpart at the position of the extended contours. We searched both the SDSS data (smoothing the FITS files so as to increase sensitivity to low surface brightness features) and the deeper NGVS data (Ferrarese et al. 2012).

Since this is an exceptionally bright galaxy with a peak S/N of 140, beam smearing is extremely strong and makes it difficult to estimate the length and velocity width of the stream. The furthest point of the extension is about 3.5 Arecibo beams at 4σ , or 60 kpc, from the center of VCC 1555. It appears to be present in 25 velocity channels, though we stress that this is uncertain, as it is difficult to rigorously define where the disk ends and the stream begins (in some channels, it is unclear if the “stream” is actually entirely detached from the disk). The peak flux of the stream is approximately 14σ . This galaxy was also observed with VIVA, and as with VCC 2070, there are hints of a short extension visible in the VIVA data roughly corresponding to the position of the long AGES stream, though the alignment is not quite as good as the case of VCC 2070 (see Figure 11.1).

This galaxy is shown in Figure 5 with the contour at 5σ over the velocity range 1948–2021 km s^{-1} .

A.3. VCC 2062/2066

While the stream connecting VCC 2062/2066 is well known and has already been seen in the AGES data (Taylor et al. 2013), accurate measurements are difficult since the feature is very close to the southern limit of the data. It appears to be significantly more extended than in the VIVA data but not more elongated, as shown in Figure 11.2. While the Köppen et al. (2018) model predicts that the galaxy should be stripping, the origin of the gas in this case is less clear. VCC 2062 is too small, VCC 2066 is a lenticular (which are generally gas-poor in Virgo; see Taylor et al. 2012, 2013), and the bulk of the gas is offset from VCC’s stellar component. A detailed discussion on this system is given in Duc et al. (2007).

This galaxy is shown in Figure 5 with the contour at 4σ over the velocity range 1088–1291 km s^{-1} .

A.4. VCC 888

This is a borderline sure/possible case as the stream is relatively small and only detected in 3–4 channels, with a peak flux of only 5σ , though the extension itself appears clearly different from the otherwise clean contours. The stream extends to about two Arecibo beams from the optical center of the galaxy, or 45 kpc at the GOLDMine distance of 23 Mpc.

This galaxy is shown in Figure 5 with the contour at 4σ over the velocity range 1087–1123 km s^{-1} .

A.5. VCC 1699

This galaxy is at the very southern edge of the AGES cube, so unfortunately, we cannot examine the whole galaxy. The extension is short, no more than two beams (35 kpc at 17 Mpc distance) but detected at the 7 – 8σ level. It appears to be somewhat less linear than the other features: while the peak S/N levels are found in the extension leading to the northwest, a possible northeastern extension is detected at the 6σ level. The northwestern extension is detected in at least eight velocity channels.

This galaxy is shown in Figure 5 with the contour at 5σ over the velocity range 1556–1735 km s^{-1} .

A.6. VCC 393

The extension here appears to be quite linear. It is relatively weak with a peak detection of 5σ , found in four velocity

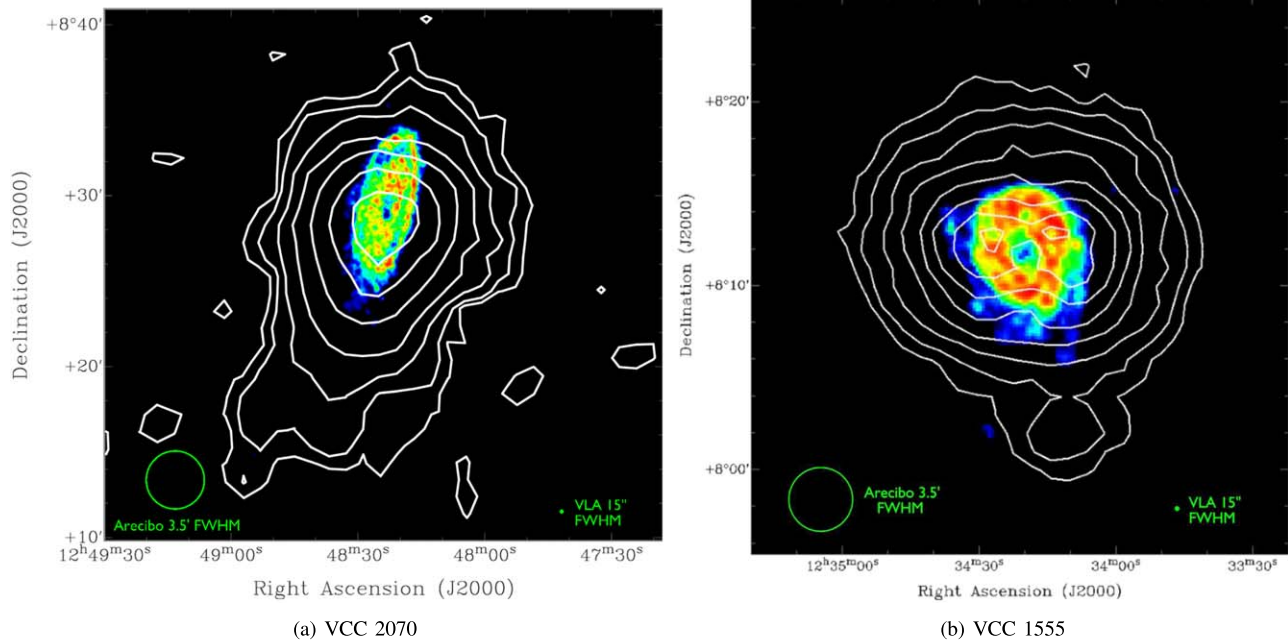


Figure 11 The two galaxies detected in the AGES VC1 data cube that were also mapped with the VIVA survey. The RGB colors show the VIVA moment 0 maps while the (logarithmically spaced) contours show the moment 0 maps from AGES. All of the 18 figure components are available in the Figure set. (The complete figure set (18 images) is available.)

channels. Its maximum extent is around two Arecibo beams or 45 kpc at its assumed 23 Mpc distance. The galaxy appears to be somewhat optically disturbed.

This galaxy is shown in Figure 5 with the contour at 4σ over the velocity range 2513–2723 km s⁻¹.

A.7. VCC 94

While the contours of this galaxy are roughly circular for most of its velocity range, over about 10 consecutive velocity channels, they are distinctly ellipsoidal, with a coherent north–south alignment. This structure is detected at a peak flux equivalent to 25σ in some channels; only the effects of beam smearing (as the galaxy itself is a bright source) caution us to give it a “sure” rather than “certain” detection rating. At the 4σ level, this source is extended up to 2.5 Arecibo beams from the galaxy’s optical center, equivalent to 80 kpc at its 32 Mpc distance.

This galaxy is shown in Figure 5 with the contour at 6σ over the velocity range 2493–2587 km s⁻¹.

A.8. EVCC 2234 (AGESVC2 025 A and B) and NGC 4746

The western extension of EVCC 2234 is not very large, but the noncircular contours persist over three or four channels and are clearly seen at 5σ . We regard this as a reasonably secure detection. This extension was already shown in Figure 5, but Figure 11.3 reveals two other, more tentative detections in the same system. EVCC 2234 appears to be interacting with the bright spiral NGC 4746, which is just outside the VCC catalog area but almost certainly a cluster member itself. There is a hint of a possible bridge between the two galaxies, but it is present over only a few channels, so we regard this as rather tentative. The southeastern extension from NGC 4746 appears as asymmetrical noisy contours over ~ 20 channels, so it is more

secure. Given the identical line-of-sight velocities of the two galaxies, they are likely interacting.

Both of these galaxies are shown in Figure 5 with the contour at 4σ over the velocity range 1574–1991 km s⁻¹.

A.9. VCC 1859

In contrast to the EVCC 2234/NGC 4746 pair, the VCC 1859/1868 pair do not appear to be interacting. The velocity difference of the two is 630 km s⁻¹, high but not necessarily forbidding an interaction given the velocity dispersion of the cluster. VCC 1868 shows clean, circular contours, whereas VCC 1859 (a 12σ detection) shows elongated, noncircular contours. The extension is a somewhat tentative detection given its small size.

This galaxy is shown in Figure 5 with the contour at 4σ over the velocity range 1596–1746 km s⁻¹.

A.10. VCC 1205

This is a borderline noisy/sure case—the galaxy certainly has noisy contours, easily visible at 4σ in Figure 11.4, but they are distinctly one-sided. We have therefore assumed in the text that this galaxy is actually another case of a tail, albeit a rather ragged one compared to the others. Contours in the figure are shown over the velocity range 2184–2475 km s⁻¹.

A.11. VCC 1249

This is a unique case of displaced gas, discussed in T12 Section 4.7 and Figure 21. Briefly, while no gas is detected at the optical position of VCC 1249 itself (Table 2 gives the upper limit from AGES), an HI cloud (AGESVC1 281, though it was previously detected in many other observations) is found midway between VCC 1249 and the nearby M49. Tables 1 and 3 give the HI mass for the cloud. The expected HI mass for the

galaxy is $4.5 \times 10^8 M_{\odot}$, so the cloud accounts for only about 10% of the missing gas.

A.12. VCC 667

This is a weak stream only visible at 3σ (Figure 11.5). Several other galaxies are found in its immediate vicinity: VCC 657 (760 km s^{-1}), 672 (922 km s^{-1}), 697 (1230 km s^{-1}), and 731 (1242 km s^{-1}). The positional alignment of VCC with the stream and its close velocity match to VCC 667 (1405 km s^{-1}) suggest a possible tidal interaction.

This galaxy is shown in Figure 11.5 with the contour at 3σ over the velocity range $1313\text{--}1542 \text{ km s}^{-1}$.

A.13. AGESVC1 204

A flat, edge-on blue galaxy with noncircular contours (visible at 5σ) that are elongated north–south (Figure 11.6). Two of the nearby galaxies (VCC 265 and 264) have velocities $> 3000 \text{ km s}^{-1}$ and are, therefore, not physically associated with the galaxy. VCC 222 is at 2410 km s^{-1} whereas AGESVC1 204 is at 2210 km s^{-1} , suggesting that a possible physical association though the tail from VCC 204 is rather short and one-sided.

This galaxy is shown in Figure 11.6 with the contour at 3σ over the velocity range $2121\text{--}2299 \text{ km s}^{-1}$.

A.14. VCC 199

VCC 199 is an early-type spiral with a relatively weak H I detection (Figure 11.7). At 4σ , its contours tentatively suggest a short extension to the northeast; however, it may be that the galaxy is simply marginally resolved with a slightly asymmetric velocity profile. However, the nearby galaxy VCC 222 is at a similar velocity (2306 km s^{-1}) to VCC 199 (2603 km s^{-1}) and well aligned with the long axis of the possible extension.

This galaxy is shown in Figure 11.7 with the contour at 5σ over the velocity range $2340\text{--}2896 \text{ km s}^{-1}$.

A.15. AGESVC1 232

This is a small blue dwarf galaxy with a possible northwest extension (Figure 11.8). This is a very uncertain detection as it is short, weak (4σ), and only present in a couple of velocity channels.

This galaxy is shown in Figure 11.8 with the contour at 4σ over the velocity range $1196\text{--}1295 \text{ km s}^{-1}$.

A.16. VCC 1011

VCC 1011 is a spiral galaxy with a possible extension aligned with the plane of its disk (Figure 11.9). The extension is rather pronounced but only visible at 4σ in a few channels. The nearby galaxy VCC 989 is at 1846 km s^{-1} so is unlikely to be associated with VCC 1011 (at 867 km s^{-1}). The dwarf galaxy AGESVC1 234 is also nearby and rather closer in velocity at 1184 km s^{-1} but shows no sign of any extensions itself.

This galaxy is shown in Figure 11.9 with the contour at 4σ over the velocity range $786\text{--}968 \text{ km s}^{-1}$.

A.17. VCC 688

This spiral galaxy shows a $3\text{--}4\sigma$ hint of asymmetrically noisy contours on its northeastern side (Figure 11.10). It is $20'$ (100 kpc) due north of AGESVC1 232, which, as mentioned, also has a hint of an extension and is at a similar velocity, but no other galaxies are visible nearby.

This galaxy is shown in Figure 11.10 with the contour at 3σ over the velocity range $1043\text{--}1230 \text{ km s}^{-1}$.

A.18. VCC 740

The extension on this irregular galaxy (Figure 11.11) is visible at 4σ with hints at 5σ . It appears to be significantly large and asymmetrical in comparison to the galaxy itself but is only visible over a few velocity channels. The bright spiral VCC 713, which has its own hint of an extension, is visible nearby. VCC 713 is at 1138 km s^{-1} whereas VCC 740 is at 877 km s^{-1} . The stream of VCC 713 runs due south, making it unclear if these two galaxies are interacting.

This galaxy is shown in Figure 11.11 with the contour at 4σ over the velocity range $797\text{--}968 \text{ km s}^{-1}$.

A.19. VCC 713

VCC 713 is a bright, red spiral that has just been detected by AGES and is strongly H I deficient. Its stream extends due south (Figure 11.12), and although it is significantly extended and detected at 5σ , it is only present in a couple of channels. Given the high predicted mass lost from this galaxy and the absence of a massive stream, it might be on its second orbit so that the stream has long since dispersed.

This galaxy is shown in Figure 11.12 with the contour at 4σ over the velocity range $1012\text{--}1261 \text{ km s}^{-1}$.

A.20. VCC 1725

At 4σ and only about one beam length across, this stream is a tentative detection at best. It appears in $3\text{--}4$ velocity channels, though rather more at 3σ . No other galaxies are visible nearby.

This galaxy is shown in Figure 11.13 with the contour at 4σ over the velocity range $1004\text{--}1196 \text{ km s}^{-1}$.

A.21. GLADOS 001

The detection of the extension from this dwarf irregular is marginal at best, visible at 4σ in only $2\text{--}3$ channels (Figure 11.14). There are no obvious galaxies that could be tidally interacting.

This galaxy is shown in Figure 11.14 with the contour at 4σ over the velocity range $2634\text{--}2718 \text{ km s}^{-1}$.

A.22. VCC 514

This small, faint spiral has a possible extension to the west, visible at 4σ in four channels (Figure 11.15). No companion galaxies are visible.

This galaxy is shown in Figure 11.15 with the contour at 4σ over the velocity range $807\text{--}903 \text{ km s}^{-1}$.

A.23. AGESVC1 235

AGESVC1 235 is a small blue dwarf galaxy with a possible roughly north–south extension, visible at 5σ in three velocity channels. VCC 393, a disturbed spiral galaxy, is only a few

arcminutes directly north, but its velocity of 2618 km s^{-1} is quite different to that of AGESVC1 235 (1667 km s^{-1}). AGESVC1 127 is also close on the sky, but is a background galaxy with a velocity $>7000 \text{ km s}^{-1}$.

This galaxy is shown in Figure 11.16 with the contour at 4σ over the velocity range $1638\text{--}1706 \text{ km s}^{-1}$.

A.24. AGESVC2 063

While the HI signal itself is secure, this stream (Figure 11.17) is only visible at σ and is only present over a few channels. If confirmed, this could be evidence of a dwarf galaxy experiencing ram pressure stripping, but we caution that the appearance of a stream could simply be due to noise.

This galaxy is shown in Figure 11.17 with the contour at 3σ over the velocity range $1837\text{--}1926 \text{ km s}^{-1}$.

A.25. VCC 1972

The spiral galaxy VCC 1972 is detected as AGESVC2 022. The HI appears to be entirely associated with the spiral rather than the nearby elliptical galaxy VCC 1978, which has a 300 km s^{-1} lower velocity. While the main extension(s) appear to point away from VCC 1978, a possible weak extension heads in the opposite direction. The nature of the extended emission is somewhat ambiguous as it is unclear whether this represents a stream or noisy contours.

This galaxy is shown in Figure 11.18 with the contour at 4.5σ over the velocity range $1205\text{--}1572 \text{ km s}^{-1}$.

ORCID iDs

Pavel Jáchym  <https://orcid.org/0000-0002-1640-5657>
 Robert Minchin  <https://orcid.org/0000-0002-1261-6641>
 Jan Palouš  <https://orcid.org/0000-0001-6729-2851>
 Richard Wunsch  <https://orcid.org/0000-0003-1848-8967>

References

- Auld, R., Minchin, R. F., Davies, J. I., et al. 2006, *MNRAS*, 371, 1617
 Bekki, K., Koribalski, B. S., & Kilborn, V. A. 2005, *MNRAS*, 363, 21
 Boselli, A., Cuillandre, J. C., Fossati, M., et al. 2016, *A&A*, 587, 68
 Boselli, A., Epinat, B., Contini, T., et al. 2019, *A&A*, 631, A114
 Boselli, A., Fossati, M., Consolandi, G., et al. 2018, *A&A*, 620, 164
 Boselli, A., & Gavazzi, G. 2006, *PASP*, 118, 517
 Chung, A., van Gorkom, J. H., Kenney, J. D. P., Crowl, H., & Vollmer, B. 2009, *AJ*, 138, 1741
 Chung, A., van Gorkom, J. H., Kenney, J. D. P., & Vollmer, B. 2007, *ApJ*, 659, 115
 Duc, P. A., & Bournaud, F. 2008, *ApJ*, 673, 787
 Duc, P. A., Braine, J., Lisenfeld, U., Brinks, E., & Boquien, M. 2007, *A&A*, 475, 187
 Espada, D., Verdes-Montenegro, L., Huchtmeier, W. K., et al. 2011, *A&A*, 532, 117
 Ferrarese, L., Côte, P., Cuillandre, J. C., et al. 2012, *ApJ*, 200, 4
 Gavazzi, G., Consolandi, G., Gutierrez, M. L., Boselli, A., & Yoshida, M. 2018, *A&A*, 618, 130
 Gavazzi, G., Giovanelli, R., Haynes, M. P., et al. 2008, *A&A*, 482, 43
 Giovanelli, R., & Haynes, M. P. 1989, *ApJ*, 346, 5
 Giovanelli, R., Haynes, M. P., Kent, B. R., et al. 2005, *AJ*, 130, 2598
 Grossi, M., Giovanardi, C., Corbelli, E., et al. 2008, *A&A*, 487, 161
 Gunn, J. E., & Gott, R. J. 1972, *ApJ*, 176, 1
 Haynes, M. P., & Giovanelli, R. 1984, *AJ*, 89, 7
 Haynes, M. P., & Giovanelli, R. 1986, *ApJ*, 306, 466
 Jáchym, P., Palouš, J., Köppen, J., & Combes, F. 2007, *A&A*, 472, 5
 Jáchym, P., Palouš, J., Köppen, J., & Combes, F. 2009, *A&A*, 500, 692
 Jaffé, Y., Smith, R., Candlish, G. M., et al. 2015, *MNRAS*, 448, 1715
 Keenan, O. C., Davies, J. I., Taylor, R., & Minchin, R. F. 2016, *MNRAS*, 456, 951
 Kent, B. 2010, *ApJ*, 725, 2333
 Kent, B., Spekkens, K., Giovanelli, R., et al. 2009, *ApJ*, 691, 1595
 Koopmann, R. A., Giovanelli, R., Haynes, M. P., et al. 2008, *ApJL*, 682, L85
 Köppen, J., Jáchym, P., Taylor, R., & Palouš, J. 2018, *MNRAS*, 479, 4367
 Minchin, R., Davies, J. I., Disney, M., et al. 2007, *ApJ*, 670, 1056
 Minchin, R. F., Auld, R., Davies, J. I., et al. 2016, *MNRAS*, 455, 3430
 Minchin, R. F., Momjian, E., Auld, R., et al. 2010, *AJ*, 140, 1093
 Minchin, R. F., Taylor, R., Köppen, J., et al. 2019, *AJ*, 158, 121
 Noordermeer, E., van der Hulst, J. M., Sancisi, R., Swaters, R. A., & van Albada, T. S. 2005, *A&A*, 442, 137
 Oosterloo, T., & van Gorkom, J. 2005, *A&A*, 437, 19
 Pisano, D. J., Wilcots, E. M., & Liu, C. T. 2002, *ApJ*, 142, 161
 Portas, A., Scott, T. C., Brinks, E., et al. 2011, *ApJ*, 739, 27
 Putman, M. E., de Heij, V., Staveley-Smith, L., et al. 2002, *AJ*, 123, 873
 Ramírez-Moreta, P., Verdes-Montenegro, L., & Blasco-Herrera, J. 2018, *A&A*, 619, 163
 Rhee, J., Smith, R., Choi, H., et al. 2017, *ApJ*, 843, 128
 Roediger, E., & Brüggem, M. 2008, *MNRAS*, 388, 465
 Ruppen, M. P. 1999, in ASP Conf. Ser. 180, Synthesis Imaging in Radio Astronomy II, A Collection of Lectures from the Sixth NRAO/NMIMT Synthesis Imaging Summer School, ed. G. B. Taylor, C. L. Carilli, & R. A. Perley (San Francisco, CA: ASP), 229
 Scott, T. C., Brinks, E., Cortese, L., Boselli, A., & Bravo-Alfaro, H. 2018, *MNRAS*, 475, 4648
 Scott, T. C., Sengupta, C., Verdes Montenegro, L., et al. 2014, *A&A*, 567, 56
 Solanes, J. M., Giovanelli, R., & Haynes, M. P. 1996, *ApJ*, 461, 609
 Solanes, J. M., Manrique, A., García-Gómez, C., González-Casado, G., Giovanelli, R., & Haynes, M. P. 2001, *ApJ*, 548, 97
 Sorgho, A., Hess, K., Carignan, C., & Oosterloo, T. 2017, *MNRAS*, 464, 530
 Swaters, R. A., van Albada, T. S., van der Hulst, J. M., & Sancisi, R. 2002, *A&A*, 390, 829
 Taylor, M. B. 2006, in ASP Conf. Ser. 351, Astronomical Data Analysis Software and Systems XV, ed. C. Gabriel et al. (San Francisco, CA: ASP), 666
 Taylor, R. 2015, *A&C*, 13, 67
 Taylor, R., Auld, R., Davies, J. I., & Minchin, R. F. 2012, *MNRAS*, 423, 787
 Taylor, R., Davies, J. I., Jáchym, P., et al. 2016, *MNRAS*, 461, 300
 Taylor, R., Davies, J. I., Jáchym, P., et al. 2017, *MNRAS*, 467, 3648
 Taylor, R., Minchin, R. F., Herbst, H., et al. 2013, *MNRAS*, 428, 459
 Taylor, R., Minchin, R. F., Herbst, H., & Smith, R. 2014, *MNRAS*, 442, 46
 Taylor, R., Wunsch, R., & Palouš, J. 2018, *MNRAS*, 479, 377
 Tonnesen, S., & Bryan, G. L. 2010, *ApJ*, 709, 1203
 Toomre, A., & Toomre, J. 1972, *ApJ*, 178, 623
 Verdugo, C., Combes, F., Dasyra, K., Salomé, P., & Braine, J. 2015, *A&A*, 582, 6
 Vollmer, B., Cayatte, V., Balkowski, C., & Duschl, W. J. 2001, *ApJ*, 561, 708
 Vollmer, B., & Huchtmeier, W. 2007, *A&A*, 462, 93
 Wang, J., Koribalski, B. S., Serra, P., et al. 2016, *MNRAS*, 460, 2143
 Yun, K., Pillepich, A., Zinger, E., et al. 2019, *MNRAS*, 483, 1082